

How colloidal surface additivation of polyamide 12 powders with well-dispersed silver nanoparticles influences the crystallization already at low 0.01 vol%

Tim Hupfeld^a, Alexander Sommereyns^{b,c}, Thomas Schuffenhauer^{c,e}, Evgeny Zhuravlev^d, Moritz Krebs^a, Stan Gann^a, Olaf Keßler^d, Michael Schmidt^{b,c}, Bilal Gökce^{a,*}, Stephan Barcikowski^a

^a Technical Chemistry I and Center for Nanointegration Duisburg-Essen (CENIDE), University of Duisburg-Essen, Universitätsstrasse 7, 45141, Essen, Germany

^b Institute of Photonic Technologies (LPT), Friedrich-Alexander Universität Erlangen-Nürnberg, Konrad-Zuse-Str.3-5, 91052, Erlangen, Germany

^c Erlangen Graduate School in Advanced Optical Technologies (SAOT), Friedrich-Alexander Universität Erlangen-Nürnberg, Germany

^d Chair of Materials Science, University of Rostock, 18051, Rostock, Germany

^e Bayerisches Laserzentrum GmbH (blz), Konrad-Zuse-Straße 2-6, 91052 Erlangen, Germany

ARTICLE INFO

Keywords:

Nanocomposite
Surface functionalization
Electrostatic deposition
Laser ablation in liquid (LAL)
Laser powder bed fusion (PBF-LB)
Selective laser sintering (SLS)
Fast scanning calorimetry (FSC)

ABSTRACT

As Additive Manufacturing (AM) is fast-growing, properties adaption of feedstock materials for AM is becoming more and more relevant due to high quality standards in industrial applications. Compared to traditional manufacturing techniques like injection molding, laser powder bed fusion (PBF-LB) of polymers has a very limited variety of processable materials, which is a major obstacle for future growth. Nanocomposites are an established material class for addressing the limitations in PBF-LB but often show poor dispersion of the nanomaterial in/on the polymer powder. Especially in the context of plasmonic nanomaterials and composites, where the state of aggregation considerably influences the optical properties, dispersion plays an important role. Our study presents a deeper understanding of the colloidal surface additivation of polyamide 12 (PA12) powders with laser-generated plasmonic silver nanoparticles, leading to high dispersion of the nanoparticles on the micropowder surface with good reproducibility. The additivation is ruled by colloidal stability and control of electrostatic forces between particles and resulted in powders that could successfully be processed on a PBF-LB machine to generate plasmonic-functionalized parts. Finally, we introduce the surface specific nanoparticle dose (surf%) as scaling key parameter complementary to the commonly used mass specific dose (wt%) to appropriately describe nanoparticle load, proving the effect of such surface additivation on the recrystallization behavior of PA12. Via flash calorimetry, already at 0.01 vol% silver load, significant nanoparticle-induced heterogeneous nucleation effects are evident, whereas the thermal properties analyzed by conventional calorimetry remain unaffected.

1. Introduction

Laser powder bed fusion (PBF-LB, according to ISO/ASTM DIS 52900:2018) of polymers, metals, or composites has become an important additive manufacturing technique for prototyping [1,2] and also started to approach serial production [3,4] due to its high geometrical flexibility and design freedom [5]. PBF-LB is more and more established in industry and a wide variety of reliable machines is available. Nowadays, the focus is shifting towards material development, since the availability of specialized powders for PBF-LB is a limiting factor for future growth [6–9]. One way of modifying powders

for PBF-LB and to affect their melting and resolidification characteristics and the mechanical properties of the final part is the additivation with inorganic micro- and nanoparticles such as carbon nanostructures [10–13] or oxides [14,15]. Such nanoscale fillers in a low amount can significantly influence the crystallization behavior through heterogeneous nucleation [16] and thus affect the mechanical properties of processed parts [10,17–19]. At the same time, induced crystallization through an increased number of nuclei can negatively affect the thermal processing characteristics of the polymer composites for PBF-LB by reducing the processing window through an increase in crystallization temperatures [20–22]. Therefore, a balanced amount of

* Corresponding author.

E-mail address: bilal.goekce@uni-due.de (B. Gökce).

<https://doi.org/10.1016/j.addma.2020.101419>

Received 9 February 2020; Received in revised form 7 June 2020; Accepted 23 June 2020

Available online 25 June 2020

2214-8604/ © 2020 Elsevier B.V. All rights reserved.

nanoparticles for maintaining a good processability and achieving desired mechanical properties has to be found. During the PBF-LB process, heating rates up to 10^7 K/min by laser radiation [23–25] and cooling rates between 0.2 and 20 K/min [26] can occur, depending on the position of the part in the process chamber. During the cooling step, spherulite (γ -phase) formation of PA12 typically originates by lamellar growth from nuclei, while increasing the overall crystallinity via primary and secondary crystallization [24,27–29]. Next to existing nuclei, the shape and quantity of the crystalline structures are also influenced by cooling rates [27,30].

Besides manipulation of crystallization behaviors, it is also possible to significantly adjust the absorption properties of the powder for wavelengths in the Vis and NIR by the addition of low amounts (0.01 wt%) of plasmonic nanomaterials [31], thus enabling inexpensive and compact diode laser PBF without the characteristic black appearance of a carbon additivated feedstock materials. Similar approaches for development of plasmonic-enhanced feedstock materials were demonstrated for two-photon polymerization [32] or near-field-enhanced laser sintering of semiconductors [33], both based on plasmonic gold nanoparticles. In contrast to gold nanoparticles, silver nanoparticles are factor 40 cheaper and come with a 4-times higher molar absorbance coefficient [34–36]. Their optical properties can further be tuned by alloying [35] and change of particle morphology [37]. In addition, composites based on silver nanostructures are known for a wide range of application [38], e.g. in biomedicine [39], electronics [40] and catalysis [41]. Therefore, the development of silver additivated feedstock materials could lead to novel properties through direct functionalization of final parts.

In this context, however, the dispersion (distribution) of the nanoparticles in the polymer matrix plays a decisive role. The poorer the dispersion and the larger and more aggregated the nanoparticles, the less nanoparticle surface is available at a given mass loading. Therefore, not only the value of the mass loading but also the degree of dispersion plays a crucial role in the nucleation properties [13,42]. The degree of nanoparticle dispersion and the surface coverage have only rarely been studied in the literature. Furthermore, the dispersion quality is deeply related to the additivation method [13,43]. Common additivation methods like dry-coating or melt compounding result in substantial aggregation of the filler after additivation [43–45]. They typically use aggregated nanoparticle, usually fabricated by gas phase synthesis (e.g., SiO_2 flow aid additive), which cannot be fully dispersed during the additivation process.

A promising method to increase the nanoparticle dispersion on microparticle surfaces is the colloidal additivation with surfactant-free laser-generated nanoparticles, which was recently demonstrated for nanoparticles on PA12 [46,68] and steel powders [15,47]. Laser synthesis and processing of colloids (LSPC) [48] can be used to synthesize a variety of nanoparticle materials in liquids. It is an easily scalable [49] and economically feasible [50] method to produce stable colloids for different applications such as composites [51], optics [33], biomedicine [52] or catalysis [53]. Additivation of polymer powders for PBF-LB is performed directly in an aqueous solution, where a laser-generated colloid and the polymer microparticles are simply mixed, followed by filtration and drying. This colloidal additivation route was initially established for the production of heterogeneous catalysts, where typically metal nanoparticles are adsorbed on support particles [54–58]. By controlling the pH during the adsorption an almost 100 % yield of this supporting procedure can be achieved and aggregation of the nanoparticles on the support can be avoided [59]. For the adsorption of nanoparticles on polymer powders, however, the mechanism for supporting in not fully understood. Therefore, influencing factors such as zeta potential, pH dependency and surface specific nanoparticle dosage need more attention.

In the present study we focus on these aspects, analyse the influence of process variables and aim for a better understanding of the particle supporting procedure. In this context, silver nanoparticles will act as a

model material, because the generation of electrostatic stabilized silver colloids by means of laser ablation is well established and the adsorption of plasmonic silver nanoparticles on polymer surfaces allows investigation of dispersion quality and quantity by optical means (characteristic surface plasmon resonance peak) and electron microscopy (good contrast of silver nanoparticles on/in polymer matrix). Since these particles might act as a nucleating agent, an impact on the calorimetric properties is expected. According to this, analysis of the surface-functionalized feedstock material is performed by differential scanning calorimetry (DSC) and fast scanning calorimetry (FSC) in order to investigate the influence of small doses of highly dispersed silver nanoparticles. To highlight the relevance of this surface-functionalized feedstock material for PBF-LB, an exemplary build job will be conducted.

2. Material and methods

2.1. Nanoparticle synthesis and colloidal additivation

Laser ablation in aqueous sodium citrate solution (100 $\mu\text{mol/l}$) was performed with a pulsed Nd:YAG-laser (Edgewave InnoSlab Laser IS400) centered at 1064 nm (8 ns, 110 W, 5 kHz), which was focused with an f-theta lens on a silver target mounted in a flow chamber setup. Small amounts of additives such as sodium citrate are known to increase colloidal stability and the reproducibility of laser-synthesis [60]. With our setup, nanoparticle synthesis by laser ablation resulted in a productivity of 1.1 g nanoparticles per hour, equivalent to more than 20 L of colloid. pH dependent zeta potential of laser-generated silver colloids was measured with PSS-Nicomb 380 ZLS after adjusting the pH with hydrochloric acid or sodium hydroxide solution. For colloidal additivation of PA12 with silver nanoparticles, PA12 (Evonik VESTO-SINT 3D Z2773, $d_{50,3} = 57.8 \mu\text{m}$, see supporting information Fig. S3 for more details) was dispersed in the colloid by mixing for 10 s, followed by stirring for 3 min (if not stated differently). Thereafter, the mixture was filtered with a Büchner funnel and a common blue-ribbon filter. Permeates were analyzed by UV-vis absorbance spectroscopy (Thermo Scientific Evolution 201) in the range of 300–900 nm (1 nm step size). As the most important parameter, the characteristic SPR peak intensity of silver at around 400 nm is analyzed. The efficiency of the supporting process is calculated by comparing the SPR intensity of the educt colloid and the permeate after additivation and filtration. It is defined as:

Supporting efficiency

$$= \frac{\text{SPR peak height (Educt)} - \text{SPR peak height (Permeate)}}{\text{SPR peak height (Educt)}} \cdot 100\% \quad (1)$$

The filter cake was dried at 50 °C for one day before size fractionation with a 125 μm sieve. Surface functionalized powders were characterized by diffuse reflection measurements (Agilent Cary 100 Bi Cricket). Distribution (Dispersion) and size of the nanoparticles on the polymer particle surface were analyzed by scanning electron microscopy (SEM, ESEM Quanta 400 FEG). In addition, transmission electron microscopy (TEM, JEOL 1400 Plus TEM) was used for high-resolution imaging of sliced polymer particles at IMCES, where samples were sliced with an ultramicrotome after being embedded in epoxy resin (EPON). Based on these images, interparticle distance histograms were extracted with the ImageJ open-source software package, counting about 400 particles, to quantify the nanoparticle dispersion [64].

Flowability was tested with a Mercury Scientific REVOLUTION Powder Analyzer and Hausner ratio were determined according to VDI 3405 Part 1.1 with a 100 mL plastic measuring cylinder by repeating the procedure four times, whereas the size of polymer particles was determined by the Camsizer X2 (ISO 13322-2) with compressed air of 50 kPa through the X-Jet extension.

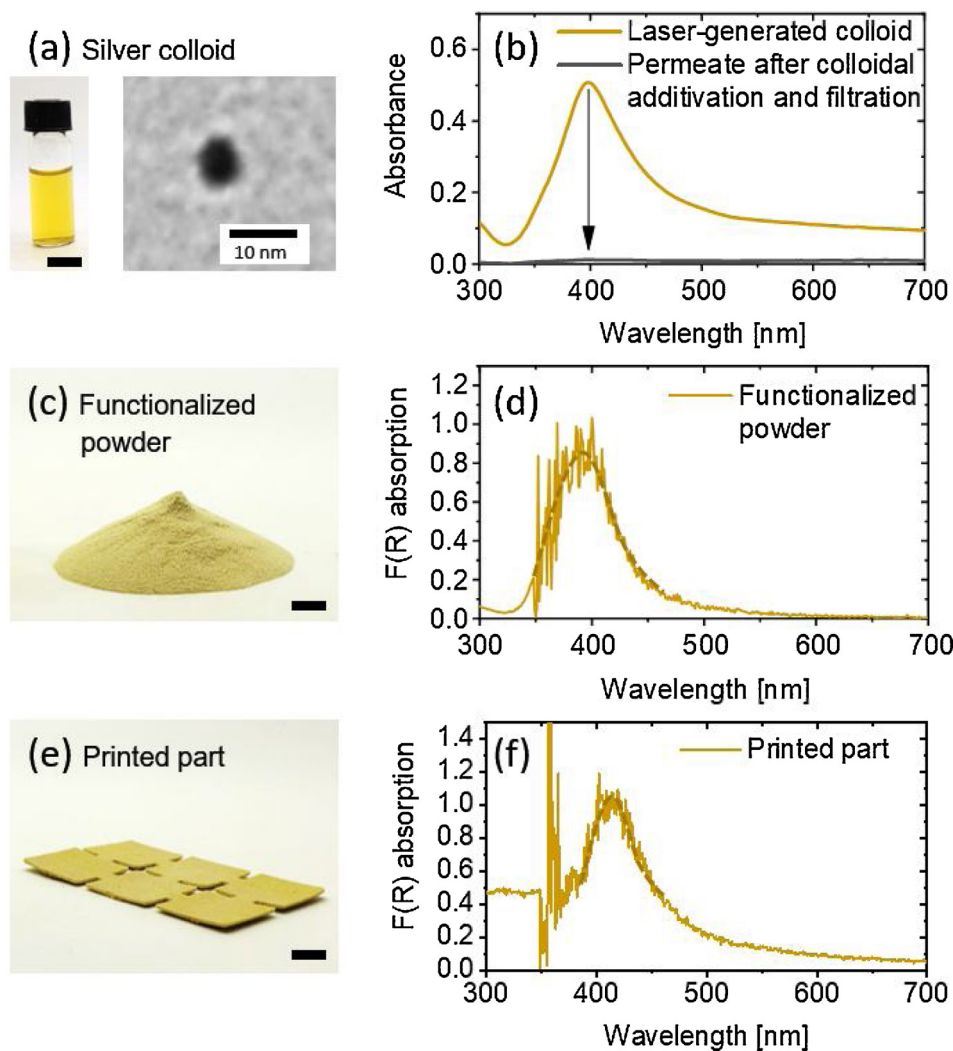


Fig. 1. Preservation of plasmonic properties along the process chain: (a) Laser-generated silver colloid with its characteristic yellow color caused by surface plasmon resonance (SPR) of silver nanoparticles and representative TEM image, and (b) corresponding UV-vis absorbance spectrum of the silver colloid showing the characteristic surface plasmon resonance peak of silver. (c) Surface-functionalized PA12 powder after filtration and drying and (d) its corresponding UV-vis absorption spectrum. (e) Test specimen after processing the powder with a Sharebot Snowwhite PBF-LB machine and corresponding UV-vis absorption spectrum. The black bar measures 1 cm.

2.2. Differential scanning calorimetry (DSC)

Surface functionalized powders were analyzed non-isothermally with a Mettler Toledo DSC 822e under nitrogen purge of 40 mL/min. Powder samples of approx. 12 mg were placed in 40 μ L aluminum pans with covers. The measurement went from 25 $^{\circ}$ C to 250 $^{\circ}$ C in a nitrogen atmosphere (nitrogen purge of 40 mL/min) with a heating rate of 10 K/min. At this temperature the samples were held for 3 min to fully melt all remaining crystals, leading to a thermal equilibrium. Afterwards, the samples were cooled down to 80 $^{\circ}$ C with a cooling rate of 10 K/min, held again for 3 min and heated up to 250 $^{\circ}$ C with 10 K/min. This way, the melting behavior of previously grown crystals as well as the sample's crystallinity can be measured. For statistical evaluation, each powder was measured three times. The evaluation of the results was performed with the Mettler Toledo STARe Evaluation Software 16.10. For the calculation of the relevant enthalpies, an integral tangential baseline was used.

2.3. Fast scanning calorimetry (FSC)

Fast scanning calorimetry was performed at the University of Rostock FSC. To cover a larger range of scanning rates which are relevant for PBF-LB and beyond, two different sensor and sample sizes were used. The calorimetric sensor XI395 with a heated area of 60 \times 80 μ m² with sample of approx. 4 ng was used to cover heating and cooling rates from 20,000–100 K/s. Heating and cooling rates from 0.1–100 K/s

were analyzed using a slower Mettler Toledo UFS 1 sensor with a heated area of 500 μ m in diameter and sample masses of approx. 40 ng were used. All measurements were performed in dry nitrogen atmosphere (-190° C).

First, samples were molten at 250 $^{\circ}$ C for 0.1 s and cooled to -190° C at 1000 K/s to have a defined thermal history. After that, samples were heated and cooled to 250 $^{\circ}$ C applying different heating and cooling rates between 0.1 and 20,000 K/s. Vittrification of pure PA12 sample occurs at cooling rates above ca. 5000 K/s – no crystallization peak and only glass transition is observed. For additivated material the critical cooling rate (cooling rate at which material becomes amorphous) was 1000 K/s. This observation is in line with larger undercooling of the additivated materials with increasing cooling rate, compared to pure PA12. As all samples showed crystallization on cooling at 1,000 K/s, the melting peak can be observed at all available heating rates up to 20,000 K/s.

After cooling at each different cooling rate, samples were reheated at 20,000 K/s to observe melting of previously formed crystals. Peak shape, temperatures, as well as enthalpy of crystallization and melting were analyzed. The absence of confinement and surface influences was confirmed by comparison of melting peaks at different heating rates (100 to 20,000 K/s) of samples with different masses.

Isothermal studies were performed using the reheating method, described in e.g. Wurm et al. [61]. Sensors XI395 with approx. 4 ng was used and samples were first molten for 0.1 s at 250 $^{\circ}$ C and then quenched to crystallization temperature at 20,000 K/s. After crystallization

for desired time it was quenched to $-190\text{ }^{\circ}\text{C}$ at maximum possible uncontrolled cooling rate (ca. 70,000 K/s at glass transition temperature) to freeze in the results of crystallization. Time of crystallization was increased logarithmically from 0.001 to 100 s. After that, reheating at 20,000 K/s was performed for melting of crystallized material. Giving the fast heating rate, reorganization of crystals was suppressed, and the overall enthalpy change during heating is equal to the previous crystallization enthalpy change. Crystallization enthalpy was compared for different temperature and time of crystallization for pure and surface-functionalized material.

3. Results and discussion

3.1. Process determinants for colloidal additivation

The colloidal additivation process starts with a laser-generated silver colloid, characterized by its yellow color, caused by the surface plasmon resonance (SPR) peak at a wavelength of 398 nm (Fig. 1a,b). The peak maximum of the number weighted particle size distribution is 4.1 nm, based on TEM particle size analysis. A representative TEM image is shown in the inset of Fig. 1a. After mixing the silver colloid with PA12 microparticles and after filtration of the mixed suspension, the permeate does not show any SPR peak (Fig. 1b) and a yellow powder remains in the filter. UV-vis absorption measurement of the dried functionalized powder (Fig. 1c) shows the characteristic SPR peak (Fig. 1d), proving the presence of nanosilver. The SPR peak wavelength of the powder is similar to the colloid and no shoulder is visible at high wavelength, indicating a successful prevention of aggregation of the silver, which would cause red-shift of SPR peak. The absence of the surface plasmon resonance peak in the permeate indicates a quantitative/high yield adsorption (supporting) of the silver nanoparticles on the surface of the polymer microparticles. Even after processing on a PBF-machine (Sharebot Snowwhite), the characteristic yellow color and the SPR peak are preserved (Fig. 1e,f). Thus, we show that the final parts were successfully functionalized with a high dispersion of plasmonic silver nanoparticles.

A deeper understanding about the kinetics of the colloidal additivation process could lead to better process control, especially in the context of upscaling towards kg-scale of functionalized powder. Since laser-generated metal colloids usually bear a high electrostatic charge with strong, pH-dependent zeta potentials [60], the pH during mixing with the polymer particles and the mixing time are suspected to be important factors for the additivation process. In a first experiment, time-dependent pH measurements were performed after mixing PA12 powder with 25 mL ultrapure water under vigorous stirring. Interestingly, the pH of the suspension changes significantly over time (Fig. 2a). Within 30 s after immersing the PA12 in water, the pH drops from pH = 6.1 to pH = 5.4, which causes the absolute zeta potential value of the silver colloid to drop from -40 mV to less than -20 mV for the silver colloid (Inset of Fig. 2a). Since the zeta potential is below an absolute value of $\pm 30\text{ mV}$, the stability of the colloid is significantly reduced, resulting in slow precipitation of the silver on the surface of the polymer microparticles. However, the pH value of the suspension is still high enough to avoid instant aggregation and a complete vanishing of the SPR peak, which is confirmed by the yellow color of the surface-functionalized. Nonetheless, the origin of the pH-shift resulting after immersing the PA12 in water remains unclear. Dissolved additives [62] like carbon acids added to the polymer powder during its processing are likely to have influence on the pH. Further results of pH measurements are provided in supporting information S1.

From Fig. 2a,b it is evident that the supporting is very fast and a supporting efficiency of $> 90\%$ is reached after less than 60 s. This was also confirmed by ICP-MS of a permeate after filtration, where approx. 10 % of the initial silver content of the educt colloid was found after supporting. Note that silver nanoparticles release ions over time which will not contribute to the SPR peak of the surface-functionalized

powders or permeates and can just be found by ICP-MS of the permeate. Further XRF analysis confirmed a silver content of $0.086 \pm 0.0015\text{ wt\%}$ in the surface-functionalized powder. A slightly smaller supporting efficiency is measured for mixing times $< 30\text{ s}$ compared to the maximum at 60 s (Fig. 2b). It is evident for our stirring conditions that supporting is faster than the change of pH, so that a critical pH range where the nanoparticles' electrostatic repulsion is almost zero is avoided. However, the necessary mixing time for $> 90\%$ supporting efficiency is likely to be affected by the batch size and stirring conditions, which is important for scale-up in order to meet the needs for PBF-LB parameter studies and build jobs. If longer mixing times were necessary, the pH value would drop further and increase the probability for aggregation.

The supporting process is also influenced by nanoparticle concentration as it is shown in Fig. 2c for the supporting efficiency and the corresponding absorption of the surface-functionalized powder (intensity of the SPR peak) at constant nanoparticle loading of 0.1 wt%. Supporting efficiency is above 95 % for all tested nanoparticle concentrations except for 10 mg/l, where the efficiency drops below 80 % and shows poor reproducibility. This could be explained by a higher stability of the colloid, since the rate of aggregation is proportional to the square of nanoparticle concentration [63]. Furthermore, smaller nanoparticle concentrations mean smaller polymer concentration in order to achieve the same polymer to nanoparticle mass ratio. As a result, the pH is higher, and the colloid is more stable, which leads to smaller supporting efficiency (see supporting information Fig. S1 information for the influence of polymer concentration on pH value). When increasing the nanoparticle concentration above 50 mg/l, supporting efficiency and powder absorption remain stable, but the probability increases to observe a complete failure of the supporting process and complete aggregation of the silver colloid. In this case the SPR peak vanishes and a greyish, almost white powder is produced, which is shown in the inset of Fig. 2c. This reproducibility issue could be explained by higher nanoparticle concentration resulting in smaller interparticle distances and weaker colloidal stability at low pH value, where repulsive forces are weaker. Two exemplary powders are depicted in the inset of Fig. 2c to illustrate the weak reproducibility. For the additivation process, especially on a larger scale, the processed volume should be as small as possible to allow smaller setups, faster filtration, and saving water. The nanoparticle concentration should, therefore, be as large as possible. As a compromise to ensure good reproducibility, a nanoparticle concentration of 50 mg/l and 60 s mixing time was used for the following experiments, which gives a polymer microparticle concentration of 50 g/l and a nanoparticle loading of 0.1 wt% (0.01 vol%) at $> 95\%$ yield.

3.2. Nanoparticle surface dose and dispersion

An essential parameter for the applications and mechanical properties of surface-functionalized powders in PBF-LB is the nanoparticle load, typically given in terms of wt%. But this value might be misleading, since the effect of nanoparticles can also be driven by their volume fraction (vol%), degree of dispersion, and surface coverage (surf %) on the polymer microparticle surface. The connection between wt%, vol%, surf% and nanoparticle size is illustrated in Fig. 3 for silver nanoparticles adsorbed on PA12 microparticles. Based on the wt%, the vol % can be calculated under consideration of the polymer and nanoparticle densities. From the wt% the theoretical surf% can be calculated as follows.

$$\begin{aligned} \text{theo. surf\%} &= \frac{\text{total nanoparticle footprint}}{\text{total polymer particle surface}} \\ &= \frac{3 \cdot \text{wt\%}}{2 \cdot A_{\text{pp}} (100 - \text{wt\%}) \cdot \delta_{\text{NP}} \cdot d_{\text{NP}}} \cdot 100\% \end{aligned}$$

A_{pp} stands for the specific surface of the polymer powder, which was calculated from the particle size distribution measured by laser

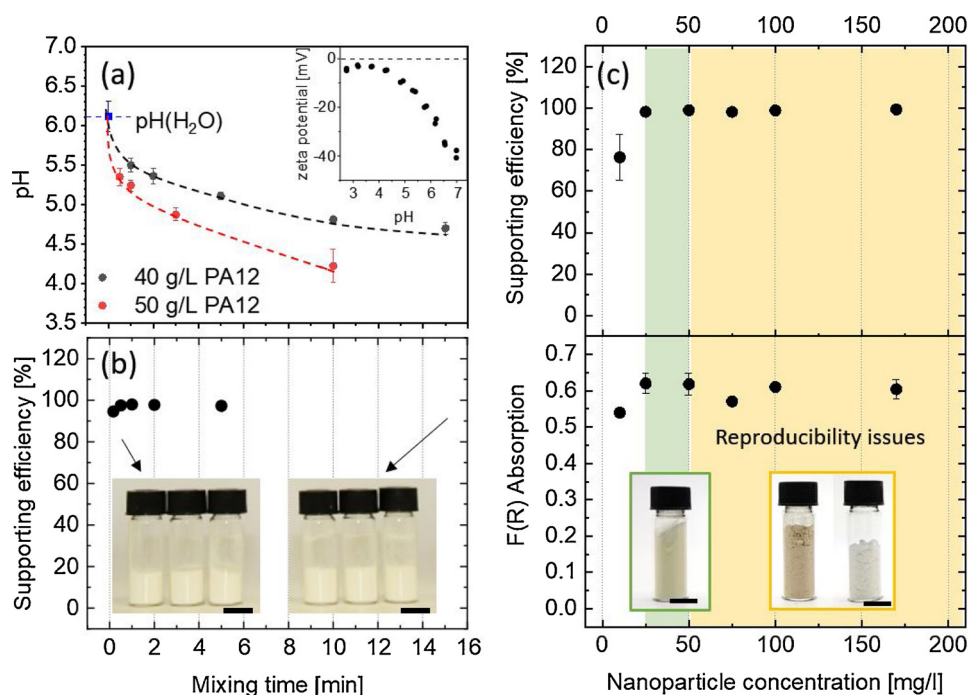


Fig. 2. Colloidal addition process characteristics: (a) pH value as a function of stirring time for PA12 dispersed in water. The inset shows the pH-dependent zeta potential of silver nanoparticles. (b) Supporting efficiency as a function of mixing time. (c) Supporting efficiency and absorption at the SPR peak of the surface-functionalized powder after drying as a function of nanoparticle concentration at a constant nanoparticle loading of 0.1 wt% (0.01 vol%). The green marked area corresponds to efficient supporting and high reproducibility, whereas the yellow area shows weaker reproducibility.

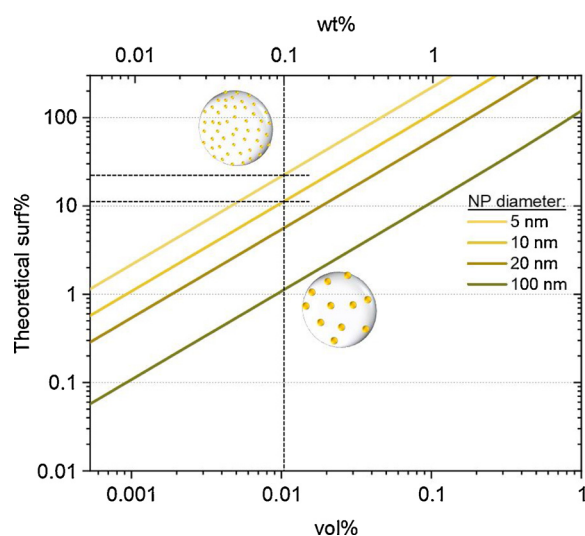


Fig. 3. Scaling graph illustrating the connection between wt%, vol%, surface coverage (surf%) and nanoparticle size for PA12 powder with a specific surface of $0.114 \text{ m}^2/\text{g}$ which was determined based on the polymer microparticle size distribution (Size distribution and different scale graphs are available in the supporting information S2). The dotted vertical line and marked range indicate a theoretical surface coverage between 10 and 20 surf% for 0.01 vol% (0.1 wt %) and nanoparticles in the range of 5 to 10 nm.

diffraction (see supporting information Fig. S2) and was equal to $0.114 \text{ m}^2/\text{g}$. δ_{NP} is the density of the nanomaterial and d_{NP} is the nanoparticle diameter. The scaling graph in Fig. 3 illustrates that far less than 1 wt% (or 0.1 vol %) of silver nanoparticles in the size of 5 nm are necessary to reach 100 % of theoretical surface coverage. If larger nanoparticles are used or if the nanomaterial aggregates on the polymer microparticle surface, the surface coverage decreases by magnitudes. This makes the surface coverage highly dependent on the dispersion and thus on the nanoaddition process itself.

The effect of high surface coverage can be observed if the wt% of nanoparticles is altered. Fig. 4a,b shows the connection between experimental supporting efficiency and theoretical surf% for a variation of

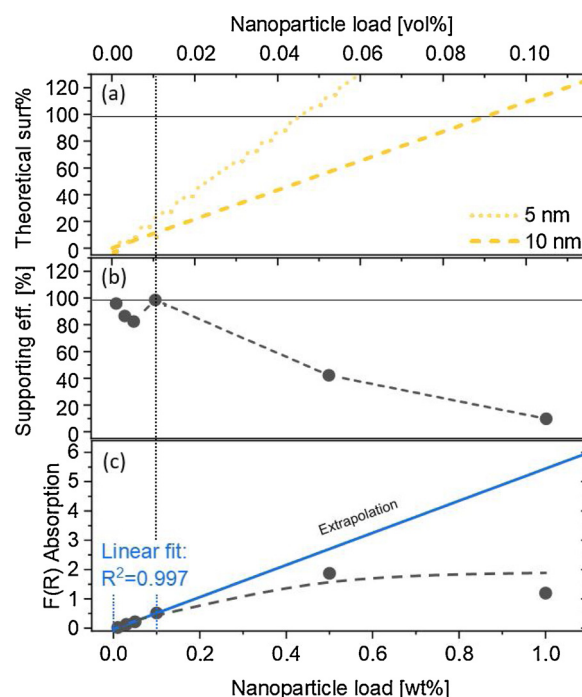


Fig. 4. (a) Theoretical surf%, (b) Supporting efficiency and SPR peak intensity (F(R) absorption) of the surface-functionalized powder as a function nanoparticle loading during colloidal addition. The dotted vertical line at 0.01 vol% mark the loading until which a linear correlation between supporting efficiency, powder absorption and nanoparticle load is observed and where a change in absorption kinetics happens.

nanoparticle loading between 0.01 and 1 wt%. The nanoparticle loading represents the ratio of silver nanoparticles and polymer microparticle during addition. If the supporting efficiency is above 80 %, which is the case until 0.1 wt%, the nanoparticle loading is approximately equal to the effective nanoparticle loading, since almost all nanoparticles are deposited on the polymer surface. This is also reflected in a linear correlation between SPR peak intensity of the powder

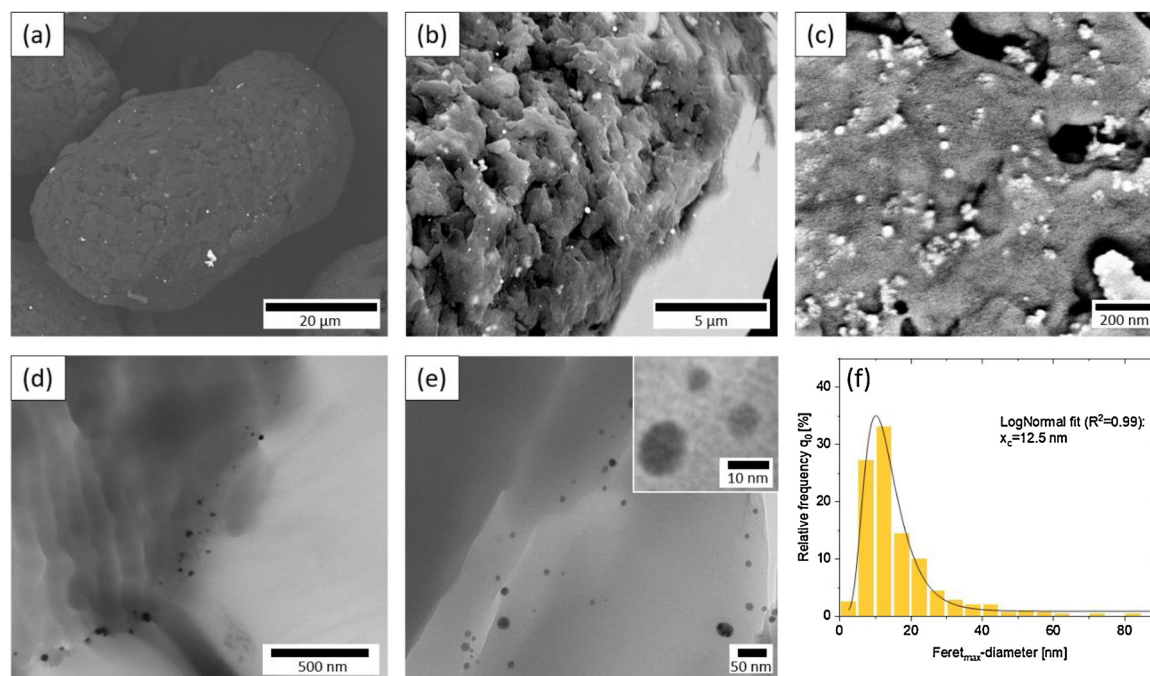


Fig. 5. (a, b, c) SEM images of PA12 microparticles decorated with 0.1 wt% silver nanoparticles. (d,e) TEM images of sliced PA12 microparticle and (f) corresponding particle size distribution ($n = 400$).

(F(R) absorption) and mass loading until 0.1 wt% (indicated by a dotted line in Fig. 4a–c). Interestingly, at higher mass loadings of 0.5 wt% and 1 wt%, the supporting efficiency decreases to 20–40 % and therefore the effective nanoparticle loading is much smaller than the theoretical value, which also results in a saturation of SPR peak intensity. For 1.0 wt% the SPR peak intensity is approximately reduced by 80 % compared to the expected value from a linear extrapolation. As expected, the decrease in supporting efficiency correlates with the threshold of maximal theoretical surface coverage which reaches 100 surf% at 0.5 wt%. This correlation can be attributed to less space on the polymer microparticle surface and hence indicates a change in absorption kinetics which results in a hindered deposition of the nanoparticles. Therefore, an increase in nanoparticle loading to more than 0.1 wt% (0.01 vol%) is not useful for the given material combination since more and more of the silver colloid would be wasted without being supported. At loadings of up to 0.1 wt% (20–40 theoretical surf%) high supporting efficiency and SPR absorption of the powder is reached.

For the additivation with 0.1 wt% nanoparticles, Fig. 5a–c shows SEM images of polymer microparticles after colloidal additivation, indicating a homogeneous distribution of nanoparticles. Silver nanoparticles exhibit only minor aggregation on the polymer microparticle surface. We also observe a high surface porosity of the PA12 microparticles which most likely results in an underestimation of the polymer particle surface assumed for the calculation of surf%. Furthermore, under consideration of the limited resolution of the SEM of approx. 10 nm, it could be possible that a significant number of nanoparticles on the polymer surface is too small to be detected by SEM. To check this hypothesis, the polymer particles were sliced and imaged via TEM. The results in Fig. 5d,e confirm the presence of small particles below 10 nm, which contribute 30 % to the total particle number (Fig. 5f, $x_c = 12.5$ nm). Thus, the primary particle diameter has not changed during additivation, which is in accordance with the conservation of the surface plasmon resonance peak. Furthermore, the polymer particle size distribution, as well as the Hausner ratio and the avalanche angle of the powder, are also not significantly influenced by additivation (Table 1), pointing at the applicability of the nano-additivated powder for PBF-LB.

3.3. Calorimetric properties

As it was shown in Fig. 3, the nanoparticle size has a significant impact on the surface coverage. Moreover, the number of small particles is of particular interest for possible effects on heterogeneous nucleation, which should depend on the particle size, especially on the presence of small non-aggregated particles with a high total surface area. Dynamic DSC analysis allows the examination and a first evaluation of the effect of nanoparticles on the thermal behavior of polymers and their influence on the relevant process window for PBF-LB. During the first heating cycle, the position of the peak, the onset and the endset, as well as its sharpness and the overall form of the melting curve show no significant difference (n.s.) between PA12 with and without silver nanoparticles (Fig. 6). Respectively, the melting peak temperature of PA12 at 185.7 ± 0.2 °C remains at 185.6 ± 0.2 °C with the addition of the silver nanoparticles. This unchanged melting behavior shows that the initial melting properties of the base polymer have not been altered through the adhesion of silver nanoparticles onto the polymer particle surface. For PBF-LB the crystallization after melting is of high interest as a read-out of the final part properties [10,64].

Nanoscale impurities inside a polymer melt are initiating a heterogeneous nucleation of spherulites during cooling [16]. Therefore, nanoparticles in the size of a crystal nuclei within a polymer melt should be able to induce a premature crystallization due to the availability of several new nucleation sites. Thermoplastic PA12 shows its typical crystallization behavior with a crystallization onset at 150.3 ± 0.3 °C (Fig. 6b). In the case of a potential nucleation effect of silver nanoparticles an earlier crystallization can be expected, and the exothermic peak should shift towards higher temperatures. Interestingly, this does not occur in our experiments (Fig. 6a). The crystallization onset of the surface-functionalized powder with 0.1 wt% silver nanoparticles lies at 150.6 ± 0.2 °C, which is not significantly different (n.s.) to the PA12 without silver nanoparticles (Fig. 6b). Respectively, the peak and the endset temperature do not significantly change with the addition of silver nanoparticles either. As a result, the addition of silver nanoparticles to PA12 retains a processing window for PBF-LB of 30 K, which is defined by the difference of the onset of the first melting and the onset of the first crystallization. Therefore, changes in crystalline

Table 1

Polymer powder particle sizes for neat PA12 and PA12 after colloidal additivition with 0.1 wt% of silver nanoparticles. dx values are given for Q0 and Q3. Powders were sieved with a 125 μm sieve before measurements. Flowability is characterized by the avalanche angle and Hausner ratio.

Samples	Particle size distribution (xarea; area of particle projection)						Avalanche angle	Hausner ratio
	x10,3	x50,3	x90,3	x10,0	x50,0	x90,0		
PA12 (washed)	42.4	57.8	72.5	0.9	4.0	8.2	48.7 \pm 0.30	1.15 \pm 0.02
PA12 + 0.1 wt% Ag	41.6	56.6	72.1	0.9	3.8	8.0	49.0 \pm 0.15	1.13 \pm 0.01

phases or nucleation effects would be detectable with a change of the overall crystallinity X_c of the samples, which can be calculated according to Eq. (2).

$$X_c = \frac{\Delta H_m}{\Delta H_{100}} \quad (2)$$

The enthalpy of fusion of the sample ΔH_m can be extracted by the data of the melting curves, while the enthalpy of fusion of a perfect PA12 crystal ΔH_{100} is given by theoretical extrapolation ($\Delta H_{100} = 209,3 \frac{\text{J}}{\text{g}}$) [65].

When heating the sample a second time, the melting peak is shifted to lower temperatures in comparison to the first melting peak due to different crystalline phases, which develop during the fabrication process of the polymer powder [27]. As a result of an isotropic crystallization during the previous cooling cycle, the enthalpy decreases from $99.5 \pm 0.5 \text{ J/g}$ to $35.25 \pm 0.1 \text{ J/g}$ and consequently, the crystallinity decreases from $47.5 \pm 0.2 \%$ to $16.8 \pm 0.1 \%$ (Fig. 6a). By adhesion of silver nanoparticles onto the PA12 powder surface, the enthalpy of fusion remains almost constant at $35.3 \pm 0.2 \text{ J/g}$ with a sample crystallinity of $16.9 \pm 0.1 \%$ and thus exhibiting no visible change in crystallization behavior from the nanoparticles at 10 K/min. In order to further investigate possible nucleation effects of silver nanoparticles within the PA12 matrix, calorimetric analysis with higher heating and cooling rates (FSC) outside of PBF conditions was conducted.

Crystallization at 150 $^{\circ}\text{C}$ occurs in the region of heterogeneous nucleation [66]. When increasing the cooling rate beyond 100 K/s, the PA 12 is crystallizing homogeneously below 100 $^{\circ}\text{C}$. It is known, that certain nucleating agents disturbs homogeneous nucleation, slowing down crystallization. To investigate the influence of additives on PA12 at faster cooling, FSC was applied. In order to extend scanning rate range, two sample sizes were used in FSC: ca. 40 ng samples cover the range 0.1–100 K/s and ca. 4 ng samples cover the range from 100 to 20,000 K/s. Fig. 7a summarizes conventional and fast scanning DSC results.

Fig. 7a shows the peak temperature for melting (dashed lines) and

crystallization (solid lines) at different heating and cooling rates. Melting was performed after cooling at cooling rate 1000 K/s. Melting peaks after 1000 K/s are almost coinciding for all samples, indicating that the thermal lag is comparable and not causing the difference for melting below 10,000 K/s. This confirms the validity of temperature measurements through all different samples in the range of scanning rates. Solid lines on Fig. 7a indicate that nanoparticle-nucleated samples crystallize at approx. 20 $^{\circ}\text{C}$ lower temperature on fast cooling compared to neat PA12. This significantly lower temperature crystallization is almost independent of the amount of nucleation agent.

PA12 shows bimodal solidification with at least two peaks (Fig. 7b). Due to DSC principles, comparison of the subtle peak development is difficult during cooling at different rates. Therefore, the reheating at 20,000 K/s was done after each cooling. The resulting heating scans for pure and 1 wt% surface-functionalized PA12 is shown in Fig. 7b. Curves shows glass transition around 52 $^{\circ}\text{C}$, followed by cold crystallization peaks at around 120 $^{\circ}\text{C}$ and melting at ca. 150 $^{\circ}\text{C}$. The melting peaks enthalpies correspond to the peak area and are comparable for the pure sample and the surface-functionalized sample, e.g. for 200 K/s cooling. But the low temperature shoulder at around 120 $^{\circ}\text{C}$ appears to be wider for the surface-functionalized PA 12. This can be interpreted as a similar crystallinity, but wider size distribution of the crystals for functionalized material.

Eventually an isothermal crystallization was performed by FSC on small samples (4 ng). Three characteristic temperatures are shown in Fig. 7c: 150 $^{\circ}\text{C}$ – temperature in the region of heterogeneous nucleation, 40 $^{\circ}\text{C}$ – temperature in the region of homogeneous nucleation and 100 $^{\circ}\text{C}$ – interplay between homogeneous and heterogeneous nucleation. Only the pure PA12 and highest nanoparticle loaded PA12 are shown here. Curves show typical sigmoidal shape with exponentially developing primary crystallization and secondary crystallization after that (for interpretation see e.g. [61]). When possible, data were fitted using Kolmogorov-Johnson-Mehl-Avrami (KJMA) kinetics [67], superimposed with linear secondary crystallization kinetics [61].

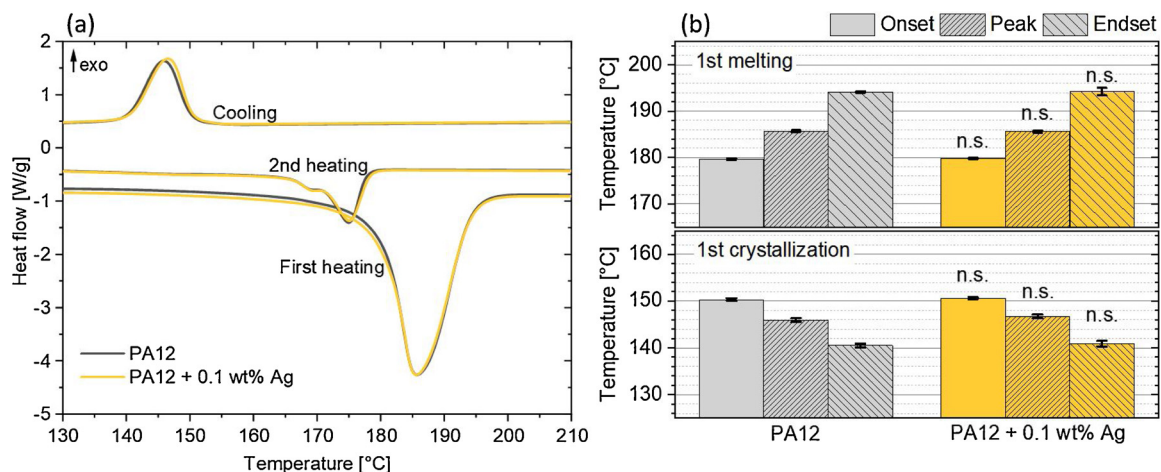


Fig. 6. Melting and crystallization curves of PA12 with and without 0.1 wt% silver nanoparticles, averaged over three runs by conventional DSC at 10 K/min. (b) Corresponding thermal values obtained from DSC of PA12 and its additivated counterpart with 0.1 wt% silver nanoparticles, based on three runs with its standard deviations and results of a significance analysis (n.s. stands for values which show no significant difference to PA12 without silver).

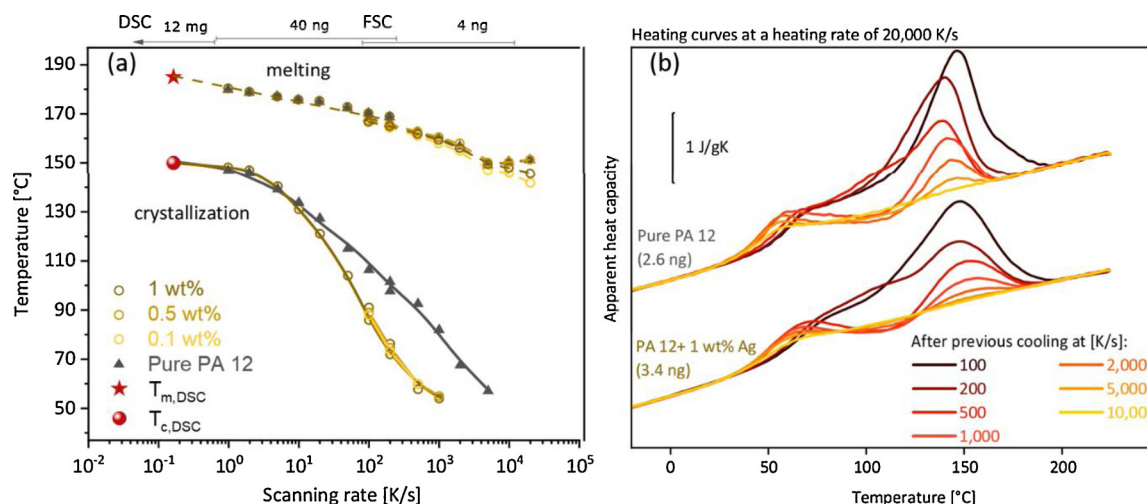


Fig. 7. Fast scanning calorimetry analysis of crystallization at low temperatures for different nanoparticle loadings. (a) Crystallization and melting peak maximum temperatures at different cooling and heating rates from 0.1 to 20,000 K/s. Melting was performed at different heating rates after cooling at 1000 K/s. Additionally, the melting and crystallization point for standard DSC measurements are highlighted in red. (b) Reheating of pure and additivated PA12 at 20,000 K/s after cooling at different rates.

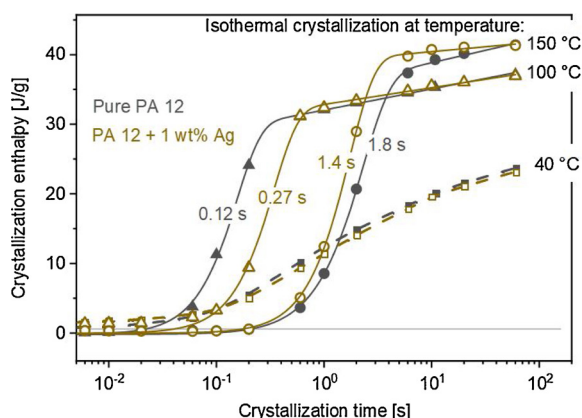


Fig. 8. Isothermal crystallization development of pure and nanoparticle-functionalized samples at three characteristic and PBF-LB relevant temperatures. Solid curves show Kolmogorov-Johnson-Mehl-Avrami (KJMA) fit and the half-time of crystallization.

Crystallization below glass transition temperature expectedly not follows Avrami kinetics and therefore were not fitted. As already observed during non-isothermal crystallization, the high temperature crystallization (150 °C in Fig. 8) shows no obvious influence of nucleation agent on crystallization half-time. In the region of homogeneous nucleation below glass transition temperature (40 °C in Fig. 8) crystallization occurs even more identically. In between (100 °C) the functionalized material is more than 2 times slower than pure PA 12. This supports the idea that as soon as the heterogeneous nucleation start to compete with homogeneous nucleation, the overall crystallization slows down.

A possible difference in the polymer-microparticle interaction could be expected for other nanoparticle material like oxides, e.g. it is known that the Hamaker constant is far lower for oxides compared to metals.

4. Conclusion

For the development of new polymer nanoparticle-composite powder materials for additive manufacturing, homogenous and fine dispersion of the nanoparticles is a key factor, which can be addressed by colloidal surface additivation. During this process, adsorption (Supporting) of silver nanoparticles on semi-crystalline PA12 powder

(Evonik VESTOSINT 3D Z2773) is a very fast process, driven by electrostatic destabilization of the colloid. Immersing the polymer powder in a laser-generated silver colloid results in a pH decrease and a supporting efficiency of more than 90 % in less than 60 s. Within this time frame, colloidal stability is still high enough to avoid aggregation effects. This is confirmed by preservation of the plasmonic properties along the process chain from the laser-generated colloid to the surface-functionalized powder and the generated test specimen after successful PBF-LB. Ideal nanoparticle and polymer concentrations were found for this process leading to high dispersion and good reproducibility. Surface coverage (surf%) of nanoparticles on the polymer surface is highly dependent on the dispersion and thus on the nano-additivation process. Saturation of plasmon resonance intensity above 0.1 wt%, can be explained with high surface coverage, more aggregation and a decrease in supporting efficiency at high mass loadings. Based on the results of the thermal analysis, silver nanoparticles clearly influence crystallization of PA12 already at 0.01 vol% (100 ppm by volume) due to the excellent dispersion of the nanoparticles, resulting in 20–40 surf %. At high temperatures and fast cooling, small amounts of silver nanoparticles preserve crystallization. However, at temperatures and cooling rates within the range of PBF-LB of polymers, silver nanoparticles show no significant effects on the crystallization behavior and thus maintain the optimal thermal properties of pure PA12 for PBF-LB. All in all, our study points a way towards a better understanding of the influence of nanoparticle surface additivation and outstanding dispersion on the functionalization of polymer powders for PBF-LB.

CRediT authorship contribution statement

Tim Hupfeld: Conceptualization, Methodology, Software, Writing - original draft, Writing - review & editing. **Alexander Sommereyns:** Methodology, Software, Writing - original draft, Writing - review & editing. **Thomas Schuffenhauer:** Data curation, Investigation. **Evgeny Zhuravlev:** Methodology, Software, Writing - original draft, Writing - review & editing. **Moritz Krebs:** Data curation, Visualization. **Stan Gann:** Data curation, Methodology. **Olaf Keßler:** Supervision, Funding acquisition, Writing - review & editing. **Michael Schmidt:** Supervision, Funding acquisition, Writing - review & editing. **Bilal Gökce:** Conceptualization, Supervision, Visualization, Funding acquisition, Writing - original draft, Writing - review & editing, Project administration. **Stephan Barcikowski:** Supervision, Funding acquisition, Writing - review & editing.

Declaration of Competing Interest

The authors declare that they have no known competing financial interests or personal relationships that could have appeared to influence the work reported in this paper.

Acknowledgements

We thank Evonik Industries for providing the PA12 powder, Smail Boukercha and Kateryna Loza (AK Epple, University of Duisburg-Essen) for SEM imaging of the polymer powders and IMCES (Imaging Center Essen, University Hospital Essen) for TEM analysis of the sliced polymer samples and fruitful discussions on nanoparticle imaging in and on polymers. The authors also thank Marc Labusch for size measurements of polymer microparticles, Milen Nachev for ICP-MS measurements of permeates and Simon Siebeneicher for his support during XRF analysis. Tim Hupfeld thanks Elisavet Papadopoulou, Leyla Carkir, Philipp P. May, Simon Nieskens and Vladyslav Sharov for their assistance during the experiments. Stan Gann thanks Markus Piechotta (Institut für Produkt Engineering, University of Duisburg-Essen) for his help during powder floability tests. The authors thank Matthias Krause (FH Dortmund, Prof. Sinnemann) for prociding first nanofunctionalized PBF-LB test specimen. Tim Hupfeld acknowledge Evonik Industries for financial support. Alexander Sommereyns gratefully acknowledges funding of the Erlangen Graduate School in Advanced Optical Technologies (SAOT) by the German Research Foundation (DFG) in the framework of the German excellence initiative. The authors gratefully acknowledge the funding by the German Research Foundation (DFG) within the priority program (SPP) 2122 "Materials for Additive Manufacturing (MATframe, BA 3580/27-1 + SCHM 2115/78-1). Bilal Gökce additionally acknowledges funding from the DFG, project GO 2566/10-1. Bilal Gökce additionally acknowledges funding from the DFG, project GO 2566/10-1.

Appendix A. Supplementary data

Supplementary material related to this article can be found, in the online version, at doi:<https://doi.org/10.1016/j.addma.2020.101419>.

References

- [1] Wohlers Associates, Wohlers Report 2019, (2019), p. 369.
- [2] T.D. Ngo, A. Kashani, G. Imbalzano, K.T.Q. Nguyen, D. Hui, Additive manufacturing (3D printing): a review of materials, methods, applications and challenges, *Compos. Part B Eng.* 143 (2018) 172–196, <https://doi.org/10.1016/j.compositesb.2018.02.012>.
- [3] Trends Appear on the Gartner Hype Cycle for Emerging Technologies, Gartner, 2019, p. 2019 (Accessed 27 September 2019), <https://www.gartner.com/smarterwithgartner/5-trends-appear-on-the-gartner-hype-cycle-for-emerging-technologies-2019/>.
- [4] P. Basiliere, 3D Printing Accelerates, 4D Printing Gets Started, Gartner, (2019) <https://blogs.gartner.com/pete-basiliere/2019/01/03/3d-printing-accelerates-4d-printing-gets-started/>.
- [5] A. Paolini, S. Kollmannsberger, E. Rank, Additive manufacturing in construction: a review on processes, applications, and digital planning methods, *Addit. Manuf.* 30 (2019) 100894, <https://doi.org/10.1016/j.addma.2019.100894>.
- [6] W. Pfefing, R. Kohler, I. Südmeyer, M. Rohde, Laser Micro and nano processing of metals, ceramics, and polymers, *Laser-Assisted Fabr. Mater.* 161 (2013) 319–374, <https://doi.org/10.1007/978-3-642-28359-8>.
- [7] F.P.W. Melchels, M.A.N. Domingos, T.J. Klein, J. Malda, P.J. Bartolo, D.W. Huttmacher, Additive manufacturing of tissues and organs, *Prog. Polym. Sci.* 37 (2012) 1079–1104, <https://doi.org/10.1016/j.progpolymsci.2011.11.007>.
- [8] Nationale Akademie der Wissenschaften Leopoldina, Deutschen Akademie der Technikwissenschaften Acatech, Additive Fertigung, Munich, 2017.
- [9] M. Schmid, A. Amado, K. Wegener, Materials perspective of polymers for additive manufacturing with selective laser sintering, *J. Mater. Res.* 29 (2014) 1824–1832, <https://doi.org/10.1557/jmr.2014.138>.
- [10] J. Bai, R.D. Goodridge, R.J.M. Hague, M. Song, Improving the mechanical properties of laser-sintered polyamide 12 through incorporation of carbon nanotubes, *Polym. Eng. Sci.* 53 (2013) 1937–1946, <https://doi.org/10.1002/pen.23459>.
- [11] R.D. Goodridge, M.L. Shofner, R.J.M. Hague, M. McClelland, M.R. Schlea, R.B. Johnson, C.J. Tuck, Processing of a Polyamide-12/carbon nanofibre composite by laser sintering, *Polym. Test.* 30 (2011) 94–100, <https://doi.org/10.1016/j.polymertesting.2010.10.011>.
- [12] T. Wagner, T. Höfer, S. Knies, P. Eyerer, Laser sintering of high temperature resistant polymers with carbon black additives, *Int. Polym. Process.* 19 (2004) 395–401, <https://doi.org/10.3139/217.1846>.
- [13] H.C. Kim, H.T. Hahn, Y.S. Yang, Synthesis of PA12/functionalized GNP nanocomposite powders for the selective laser sintering process, *J. Compos. Mater.* 47 (2012) 501–509, <https://doi.org/10.1177/0021998312441812>.
- [14] M.M. Lexow, D. Drummer, New materials for SLS: the use of antistatic and flow agents, *J. Powder Technol.* 2016 (2016) 1–9, <https://doi.org/10.1155/2016/4101089>.
- [15] C. Doñate-Buendía, F. Frömel, M.B. Wilms, R. Streubel, J. Tenkamp, T. Hupfeld, M. Nachev, E. Gökce, A. Weisheit, S. Barcikowski, F. Walther, J.H. Schleifenbaum, B. Gökce, Oxide dispersion-strengthened alloys generated by laser metal deposition of laser-generated nanoparticle-metal powder composites, *Mater. Des.* 154 (2018) 360–369, <https://doi.org/10.1016/j.matdes.2018.05.044>.
- [16] E. Piorkowska, G.C. Rutledge, Handbook of Polymer Crystallization, (2013), <https://doi.org/10.1002/9781118541838>.
- [17] S.R. Athreya, K. Kalaitzidou, S. Das, Mechanical and microstructural properties of Nylon-12/carbon black composites: selective laser sintering versus melt compounding and injection molding, *Compos. Sci. Technol.* 71 (2011) 506–510, <https://doi.org/10.1016/j.compscitech.2010.12.028>.
- [18] S. Fu, Z. Sun, P. Huang, Y. Li, N. Hu, Some basic aspects of polymer nanocomposites: a critical review, *Nano Mater. Sci.* 1 (2019) 2–30, <https://doi.org/10.1016/j.nanoms.2019.02.006>.
- [19] Y. Wang, Y. Shi, S. Huang, Selective laser sintering of polyamide-rectorite composite, *Proc. Inst. Mech. Eng. Part L J. Mater. Des. Appl.* 219 (2005) 11–16, <https://doi.org/10.1243/146442005X10229>.
- [20] D. Eiras, L.A. Pessan, Influence of calcium carbonate nanoparticles on the crystallization of polypropylene, *Mater. Res.* 12 (2009) 523–527, <https://doi.org/10.1590/S1516-14392009000400024>.
- [21] Y. Wang, C.M. Dinapoli, G.A. Tofig, R.W. Cunningham, R.A. Pearson, Selective Laser Sintering Processing Behavior of Polyamide Powders, n.d.
- [22] C. Huang, X. Qian, R. Yang, Thermal conductivity of polymers and polymer nanocomposites, *Mater. Sci. Eng. R Rep.* 132 (2018) 1–22, <https://doi.org/10.1016/j.mser.2018.06.002>.
- [23] D. Drummer, M. Drexler, K. Wudy, Impact of heating rate during exposure of laser molten parts on the processing window of PA12 powder, *Phys. Procedia* 56 (2014) 184–192, <https://doi.org/10.1016/j.phpro.2014.08.162>.
- [24] T. Laumer, K. Wudy, M. Drexler, P. Amend, S. Roth, D. Drummer, M. Schmidt, Fundamental investigation of laser beam melting of polymers for additive manufacture, *J. Laser Appl.* 26 (2014) 042003, <https://doi.org/10.2351/1.4892848>.
- [25] L. Lanzl, K. Wudy, M. Drexler, D. Drummer, Laser-high-speed-DSC: process-oriented thermal analysis of PA 12 in selective laser sintering, *Phys. Procedia* 83 (2016) 981–990, <https://doi.org/10.1016/j.phpro.2016.08.103>.
- [26] M. Zhao, K. Wudy, D. Drummer, Crystallization kinetics of polyamide 12 during Selective laser sintering, *Polymers (Basel)* 10 (2018), <https://doi.org/10.3390/polym10020168>.
- [27] M. Schmid, Laser sintering with plastics, Technology, Processes, and Materials, (2018), <https://doi.org/10.3139/9781569906842.fm>.
- [28] D. Hui, R.D. Goodridge, C.A. Scotchford, D.M. Grant, Laser sintering of nano-hydroxyapatite coated polyamide 12 powders, *Addit. Manuf.* 22 (2018) 560–570, <https://doi.org/10.1016/j.ADDMA.2018.05.045>.
- [29] F.J. Baltá-Calleja, T.A. Ezquerro, Polymer crystallization: general concepts of theory and experiments, *Encycl. Mater. Sci. Technol.* (2001) 7244–7252, <https://doi.org/10.1016/B0-08-043152-6/01289-4> Elsevier.
- [30] N.L.A. McFerran, C.G. Armstrong, T. McNally, Nonisothermal and isothermal crystallization kinetics of nylon-12, *J. Appl. Polym. Sci.* 110 (2008) 1043–1058, <https://doi.org/10.1002/app.28696>.
- [31] A.W. Powell, A. Stavrinadis, I. De Miguel, G. Konstantatos, R. Quidant, White and brightly colored 3D printing based on resonant photothermal sensitizers, *Nano Lett.* 18 (2018) 6660–6664, <https://doi.org/10.1021/acs.nanolett.8b01164>.
- [32] L. Jonušauskas, M. Lau, P. Gruber, B. Gökce, S. Barcikowski, M. Malinauskas, A. Ovsianikov, Plasmon assisted 3D microstructuring of gold nanoparticle-doped polymers, *Nanotechnology* 27 (2016) 154001, <https://doi.org/10.1088/0957-4484/27/15/154001>.
- [33] M. Lau, R.G. Niemann, M. Bartsch, W. O'Neill, S. Barcikowski, Near-field-enhanced, off-resonant laser sintering of semiconductor particles for additive manufacturing of dispersed Au-ZnO-micro/nano hybrid structures, *Appl. Phys. A Mater. Sci. Process.* 114 (2014) 1023–1030, <https://doi.org/10.1007/s00339-014-8270-1>.
- [34] Z. Yan, R.A. Shah, G. Chado, S.K. Gray, M. Pelton, N.F. Scherer, Guiding spatial arrangements of silver nanoparticles by optical binding interactions in shaped light fields, *ACS Nano* 7 (2013) 1790–1802, <https://doi.org/10.1021/nn3059407>.
- [35] A. Neumeister, J. Jakobi, C. Rehbock, J. Moysig, S. Barcikowski, Monophasic ligand-free alloy nanoparticle synthesis determinants during pulsed laser ablation of bulk alloy and consolidated microparticles in water, *Phys. Chem. Chem. Phys.* 16 (2014) 23671–23678, <https://doi.org/10.1039/C4CP03316G>.
- [36] S. Link, Z.L. Wang, M.A. El-Sayed, Alloy formation of gold-silver nanoparticles and the dependence of the plasmon absorption on their composition, *J. Phys. Chem. B* 103 (1999) 3529–3533, <https://doi.org/10.1021/jp990387w>.
- [37] V. Amendola, O.M. Bakr, F. Stellacci, A study of the surface plasmon resonance of silver nanoparticles by the discrete dipole approximation method: effect of shape, size, structure, and assembly, *Plasmonics* 5 (2010) 85–97, <https://doi.org/10.1007/s11468-009-9120-4>.
- [38] I. Pastoriza-Santos, C. Kinnear, J. Pérez-Juste, P. Mulvaney, L.M. Liz-Marzán, Plasmonic polymer nanocomposites, *Nat. Rev. Mater.* 3 (2018) 375–391, <https://doi.org/10.1038/s41578-018-0050-7>.

- [39] Y.H. Lim, K.M. Tiemann, G.S. Heo, P.O. Wagers, Y.H. Rezenom, S. Zhang, F. Zhang, W.J. Youngs, D.A. Hunstad, K.L. Wooley, Preparation and in vitro antimicrobial activity of silver-bearing degradable polymeric nanoparticles of polyphosphoester-block-poly(l-lactide), *ACS Nano* 9 (2015) 1995–2008, <https://doi.org/10.1021/nn507046h>.
- [40] R. Zhu, C.H. Chung, K.C. Cha, W. Yang, Y.B. Zheng, H. Zhou, T. Bin Song, C.C. Chen, P.S. Weiss, G. Li, Y. Yang, Fused silver nanowires with metal oxide nanoparticles and organic polymers for highly transparent conductors, *ACS Nano* 5 (2011) 9877–9882, <https://doi.org/10.1021/nn203576v>.
- [41] N. Karak, Silver Nanomaterials and Their Polymer Nanocomposites, *Nanomater. Polym. Nanocomposites*, (2019), pp. 47–89, <https://doi.org/10.1016/b978-0-12-814615-6.00002-3>.
- [42] S.R. Athreya, K. Kalaitzidou, S. Das, Processing and characterization of a carbon black-filled electrically conductive Nylon-12 nanocomposite produced by selective laser sintering, *Mater. Sci. Eng. A* 527 (2010) 2637–2642, <https://doi.org/10.1016/j.msea.2009.12.028>.
- [43] S. Yuan, F. Shen, C.K. Chua, K. Zhou, Polymeric composites for powder-based additive manufacturing: materials and applications, *Prog. Polym. Sci.* 91 (2019) 141–168, <https://doi.org/10.1016/j.progpolymsci.2018.11.001>.
- [44] C. Blümel, M. Sachs, T. Laumer, B. Winzer, J. Schmidt, M. Schmidt, W. Peukert, K.E. Wirth, Increasing flowability and bulk density of PE-HD powders by a dry particle coating process and impact on LBM processes, *Rapid Prototyp. J.* 21 (2015) 697–704, <https://doi.org/10.1108/RPJ-07-2013-0074>.
- [45] J. Yang, A. Sliva, A. Banerjee, R.N. Dave, R. Pfeffer, Dry particle coating for improving the flowability of cohesive powders, *Powder Technol.* 158 (2005) 21–33, <https://doi.org/10.1016/j.powtec.2005.04.032>.
- [46] T. Hupfeld, T. Laumer, T. Stichel, T. Schuffenhauer, J. Heberle, M. Schmidt, S. Barcikowski, B. Gökce, A new approach to coat PA12 powders with laser-generated nanoparticles for selective laser sintering, *Procedia CIRP* 74 (2018) 244–248, <https://doi.org/10.1016/j.procir.2018.08.103>.
- [47] R. Streubel, M.B. Wilms, C. Doñate-Buendía, A. Weisheit, S. Barcikowski, J.H. Schleifenbaum, B. Gökce, Depositing laser-generated nanoparticles on powders for additive manufacturing of oxide dispersed strengthened alloy parts via laser metal deposition, *J. Appl. Phys.* 57 (2018), <https://doi.org/10.7567/JJAP.57.040310>.
- [48] D. Zhang, B. Gökce, S. Barcikowski, Laser synthesis and processing of colloids: fundamentals and applications, *Chem. Rev.* 117 (2017) 3990–4103, <https://doi.org/10.1021/acs.chemrev.6b00468>.
- [49] R. Streubel, G. Bendt, B. Gökce, Pilot-scale synthesis of metal nanoparticles by high-speed pulsed laser ablation in liquids, *Nanotechnology* 27 (2016) 205602, <https://doi.org/10.1088/0957-4484/27/20/205602>.
- [50] S. Jendzej, B. Gökce, M. Epple, S. Barcikowski, How size determines the value of gold: economic aspects of wet chemical and laser-based metal colloid synthesis, *ChemPhysChem* 18 (2017) 1012–1019, <https://doi.org/10.1002/cphc.201601139>.
- [51] D. Zhang, B. Gökce, Perspective of laser-prototyping nanoparticle-polymer composites, *Appl. Surf. Sci.* 392 (2017) 991–1003, <https://doi.org/10.1016/j.apsusc.2016.09.150>.
- [52] A. Blaeser, N. Million, D.F.D. Campos, L. Gamrad, M. Köpf, C. Rehbock, M. Nachev, B. Sures, S. Barcikowski, H. Fischer, Laser-based in situ embedding of metal nanoparticles into bioextruded alginate hydrogel tubes enhances human endothelial cell adhesion, *Nano Res.* 9 (2016) 3407–3427, <https://doi.org/10.1007/s12274-016-1218-3>.
- [53] J. Zhang, M. Chaker, D. Ma, Pulsed laser ablation based synthesis of colloidal metal nanoparticles for catalytic applications, *J. Colloid Interface Sci.* 489 (2017) 138–149, <https://doi.org/10.1016/j.jcis.2016.07.050>.
- [54] S. Reichenberger, G. Marzun, M. Muhler, S. Barcikowski, Perspective of surfactant-free colloidal nanoparticles in heterogeneous catalysis, *ChemCatChem* 11 (2019) 4489–4518, <https://doi.org/10.1002/cctc.201900666>.
- [55] S. Barcikowski, P. Wagener, A. Schwenke, Method for producing micro-nano combined active systems, *US9403160B2*, 2016. doi:10.1016/j.73).
- [56] G. Marzun, J. Nakamura, X. Zhang, S. Barcikowski, P. Wagener, Size control and supporting of palladium nanoparticles made by laser ablation in saline solution as a facile route to heterogeneous catalysts, *Appl. Surf. Sci.* 348 (2015) 75–84, <https://doi.org/10.1016/j.apsusc.2015.01.108>.
- [57] M. Lau, A. Ziefuss, T. Komossa, S. Barcikowski, Inclusion of supported gold nanoparticles into their semiconductor support, *Phys. Chem. Chem. Phys.* 17 (2015) 29311–29318, <https://doi.org/10.1039/c5cp04296h>.
- [58] P. Wagener, A. Schwenke, S. Barcikowski, How citrate ligands affect nanoparticle adsorption to microparticle supports, *Langmuir* 28 (2012) 6132–6140, <https://doi.org/10.1021/la204839m>.
- [59] E. Bertin, A. Münzer, S. Reichenberger, R. Streubel, T. Vinnay, H. Wiggers, C. Schulz, S. Barcikowski, G. Marzun, Durability study of platinum nanoparticles supported on gas-phase synthesized graphene in oxygen reduction reaction conditions, *Appl. Surf. Sci.* 467–468 (2019) 1181–1186, <https://doi.org/10.1016/j.apsusc.2018.10.061>.
- [60] V. Merk, C. Rehbock, F. Becker, U. Hagemann, H. Nienhaus, S. Barcikowski, In situ non-DLVO stabilization of surfactant-free, plasmonic gold nanoparticles: effect of Hofmeister's anions, *Langmuir* 30 (2014) 4213–4222, <https://doi.org/10.1021/la404556a>.
- [61] A. Wurm, E. Zhuravlev, K. Eckstein, D. Jehnichen, D. Pospiech, R. Androsch, B. Wunderlich, C. Schick, Crystallization and homogeneous nucleation kinetics of poly(ϵ -caprolactone) (PCL) with different molar masses, *Macromolecules* 45 (2012) 3816–3828, <https://doi.org/10.1021/ma300363b>.
- [62] S. Monsheimer, M. Grebe, F.E. Baumann, W. Christoph, T. Schiffer, H. Scholten, *Laser-Sinter-Pulver mit verbesserten Recyclingeigenschaften, Verfahren zu dessen Herstellung und Verwendung des Laser-Sinter-Pulvers*, EP1413594A2, (2004).
- [63] N. Kallay, S. Žalac, Stability of nanodispersions: a model for kinetics of aggregation of nanoparticles, *J. Colloid Interface Sci.* 253 (2002) 70–76, <https://doi.org/10.1006/jcis.2002.8476>.
- [64] S. Dupin, O. Lame, C. Barrès, J.Y. Charneau, Microstructural origin of physical and mechanical properties of polyamide 12 processed by laser sintering, *Eur. Polym. J.* 48 (2012) 1611–1621, <https://doi.org/10.1016/j.eurpolymj.2012.06.007>.
- [65] S. Gogolewski, Effect of annealing on thermal properties and crystalline structure of polyamides, *Colloid Polym. Sci.* 257 (1979) 811–819 <http://www.springerlink.com/content/tu119881u5545674/>.
- [66] F. Paolucci, M.J.H. van Mook, L.E. Govaert, G.W.M. Peters, Influence of post-condensation on the crystallization kinetics of PA12: from virgin to reused powder, *Polymer (Guildf.)* 175 (2019) 161–170, <https://doi.org/10.1016/j.polymer.2019.05.009>.
- [67] A.T. Lorenzo, M.L. Arnal, J. Albuern, A.J. Müller, DSC isothermal polymer crystallization kinetics measurements and the use of the Avrami equation to fit the data: guidelines to avoid common problems, *Polym. Test.* 26 (2007) 222–231, <https://doi.org/10.1016/j.polymertesting.2006.10.005>.
- [68] Tim Hupfeld, et al., Plasmonic seasoning: Giving color to desktop laser 3D-printed polymers by highly dispersed nanoparticles, *Adv. Opt. Mater.* (2020), <https://doi.org/10.1002/adom.202000473>.